Article

Laser Welding of UNS S33207 Hyper-Duplex Stainless Steel to 6061 Aluminum Alloy Using High Entropy Alloy as a Filler Material

Dhanesh G. Mohan [1,]*, Jacek Tomków [2] and Sasan Sattarpanah Karganroudi [3]

[1] Institute of Materials Joining, Shandong University, Jinan 250061, China
[2] Institute of Manufacturing and Materials Technology, Faculty of Mechanical Engineering and Ship Technology, Gdańsk University of Technology, 80-233 Gdansk, Poland; jacek.tomkow@pg.edu.pl
[3] Department of Mechanical Engineering, University of Quebec in Trois-Rivieres, Trois-Rivieres, QC G9A 5H7, Canada; sasan.karganroudi@itmi.ca
[*] Correspondence: dhanesh@sdu.edu.cn

Abstract: The high entropy alloy (HEA) filler used during the fabrication method determines the reliability of HEAs for steel-aluminum dissimilar alloy configuration. HEAs have a direct impact on the formation of intermetallic compounds (IMC) formed by the interaction of iron (Fe) and aluminum (Al), and influence the size of the joint's interaction zone. A novel welding process for Fe-Al alloy joints was developed to prevent the development of a brittle iron-aluminum interface. This research involved investigation of the possibility of using HEA powdered filler. $Fe_5Co_{20}Ni_{20}Mn_{35}Cu_{20}$ HEAs was used as a filler for the laser joining lap configuration joining hyper-duplex stainless steel UNS S33207 to aluminum alloy 6061. This HEA has unique properties, such as high strength, good ductility, and high resistance to corrosion and wear. A tiny portion of the stainless-steel area was melted by varying the welding parameters. The high-entropy alloy (HEA) with slow kinetic diffusion and large entropy was employed to aid in producing solid solution structures, impeding the blending of iron and aluminum particles and hindering the development of Fe-Al IMCs. The weld seam was created without the use of Fe-Al IMCs,. The specimen broke at the HEAs/Al alloy interface with a tensile-shear strength of 237 MPa. The tensile-shear strength achieved was 12.86% higher than for the base metal AA 6061 and 75.57% lower than for the UNS S33207 hyper-duplex stainless steel.

Keywords: high entropy alloy; hyper-duplex stainless steel; laser welding; aluminum alloy

1. Introduction

A hybrid joint made of dissimilar metals has been a focus of research in battery case manufacturing, and in the automotive and marine sectors for a long time [1,2]. The synergistic qualities of the metals, as well as the creation of design efficient structures, are the primary driving forces behind this [3]. However, joining dissimilar metal combinations can be challenging because of inferior chemical compatibility and dissimilarities in physical properties. For example, when welding aluminum to steel, the interface between aluminum and (Al) iron (Fe) atoms throughout the welding process forms intermetallic compounds (IMCs) with high brittleness [4]. As the presence of these IMCs limits the strength of the joint, the amount of these compounds should be kept to a minimum.

Furthermore, all fusion welding methods occur in transient conditions, and the time and temperature cannot be separately controlled. Moreover, the heat cycle applied to the weldment determines the thickness of the IMC layer and the width of the weld [5,6]. Therefore, to regulate these two components, it is first necessary to understand the heat cycle and its effects.

The advantages of iron (Fe) and aluminum alloys (Al) include excellent mechanical strength and corrosion resistance. As a result, they have a wide range of uses in maritime,

automotive, and space applications [7]. Consequently, Fe-Al composite structures have received increasing interest as a means to amalgamate the positive characteristics of Fe with Al metal alloys. However, due to significant variations in material parameters, such as thermal properties, melting point, material characteristics, and grain morphology, effective Fe/Al welding conditions are hard to formulate and can generate Fe-Al phases with high brittleness [8,9].

The main benefits of laser welding compared to arc welding are: (1) by adjusting the laser metal interaction, the dimension and melt pool geometry can be controlled, which would be difficult to achieve with an arc-welding method; (2) because of the high energy density in laser welding, a nominal heat-affected zone is created; (3) higher cooling and solidification levels compared to other fusion welding methods; and (4) localized and focused heating [10–14]. Furthermore, with gas tungsten arc welding (GTAW), managing the temperature ranges is not feasible as the temperature required to melt the aluminum will only wet the steel [15–17]. Traditional non-consumable techniques, such as GTAW or plasma, would not provide such control.

Lasers are used for the cladding layers in many industries, e.g., the metal industry [18–20] and medicine [21,22]. The process is also used in water environments [23,24]. In addition, lasers are widely used in the fusion welding process to fabricate joints between duplex steel and aluminum alloys. Most studies have focused on minimizing Fe-Al IMC formation by regulating the beam offset position and distance to control the volume of the melted base material [25]. Other investigations have found that dual-beam welding improves the uniformity of IMC thickness, and that silicon helps decrease fractures in the weld. Nevertheless, none of the strategies listed above can prevent IMC development in Fe/Al interfaces. Furthermore, in dissimilar metal welding, a portion of the non-melted transitional layer remaining in the weldments butting surface will entirely avoid blending with parent materials [26].

The approach is non-ideal for lap-welding configuration with lasers [27]. As a result, novel welding processes must be investigated in order to efficiently regulate the development and growth of Fe-Al IMCs in the weld zone of the lap interface. Based on their high entropy impact, HEAs can enhance the development of solid solutions [28]. The mechanical characteristics of high-entropy alloys (HEAs) are directly connected to their structural stability. Therefore, proper monitoring of component composition is essential in understanding structural stability and determining mechanical characteristics. Co-Cr-Fe-Ni HEAs have been built using a single face-centered cubic (FCC) solid solution. Elemental components have a noticeable influence on their structure and performance; the Cr and Fe elements, in particular, have an apparent effect on structural stability and the equilibrium lattice constant. In addition, the Ni components have a noticeable impact on rigidity. According to the Pugh ratios, Cr and Ni addition may enhance ductility, but Co and Fe addition may lower it. Therefore, the structural stability and stiffness of Co-Cr-Fe-Ni HEAs are enhanced by increasing Co and Fe concentrations or reducing Cr and Ni contents. The structural stability and mechanical characteristics of Co-Cr-Fe-Ni HEAs may be attributed to the strength of the metallic bonding and covalent bonding, which is influenced by the element content variation [29].

In previous studies, the mechanical properties of the weldments have been related only to the thickness of the IMC layer, and the weld interface area among the stainless steel and aluminum has not been considered. Mechanical strength should evolve linearly with the bonding area. However, the continuous IMC layer generated at the weld surface prevents the linear trend from being observed. A thickness of the IMC layer up to 8 μm would result in sound Fe-Al joints [30–32]. Although utilizing shallow energy in the welding process to restrict IMC layer formation has a favorable impact, this method also results in the formation of a narrow bonding area with lower weld strength [33,34]. In dissimilar metal welding, the sluggish kinetic diffusion property is exploited to prevent the blending of adjacent layers. For example, using powdered HEAs as a filler metal leads to the effective joining of aluminum and austenitic stainless steel in butt configuration [35]. Nevertheless,

using HEAs as filler metals in the laser welding of dissimilar metals, such as aluminum and steel, has been little explored.

Since none of the standard filler metal compositions meet the stricter requirements of HEAs, further investigations into the competence of such alloys to perform as fillers are worthwhile, and focus has shifted in this direction. In the following, we use the Pickering and Jones convention [36,37] and label HEAs to reflect the atomic number of the elements. However, there are non-equiatomic configurations with more predominant elements in the composition over others; this results in the renaming of selected alloys. The elements are rearranged from how they were provided in their initial form.

For the welding of dissimilar alloys, such as hyper-duplex stainless steel and aluminum alloy, vanadium and niobium are frequently utilized as corresponding layers that have a substantial repressive influence upon the generation of Fe-Al IMCs. The welding stress can lessen the exceptional ductility of copper, and the coefficient of diffusion of Ni and Fe is much greater than that of Al and Fe. Supplementing Ni can interfere with the formation of IMCs formed by the combination of Fe and Al. According to HEA theory, the atomic radius of Cu, Ni, Mn, and Co are identical. Therefore, they can produce a solid solution with ease. This research presents a laser welding technique for hyper-duplex stainless steel (UNS S33207) and aluminum alloy (AA 6061) using $Fe_5Co_{20}Ni_{20}Mn_{35}Cu_{20}$ HEAs. Fe-Al IMCs are predicted to be repressed using HEAs fillers in Fe/Al lap joint configuration and to limit the melting of parent metal on the hyper duplex stainless-steel side. To date, this type of laser welding has been rarely performed.

2. Materials and Methods

2.1. Materials

Plates of UNS S33207 hyper-duplex stainless steel and AA 6061 aluminum alloy with 2 mm thickness and 100 mm length and 70 mm width were used; the length and width were chosen according to the ASTM D8172-18 standard for shear testing resistance seam welds [38]. The materials' mechanical properties and chemical composition were as per the materials certificate provided by the supplier, as detailed in Tables 1 and 2. First, the oxide layer and other surface impurities on the plates were removed by grounding the hyper duplex stainless steel and linishing the aluminum alloy. Afterwards, all plates were degreased with acetone solution.

Table 1. Mechanical properties of UNS S33207 and AA 6061.

Material	Tensile Strength [MPa]	Elongation [%]	Hardness [HV]
UNS S33207	970	25	523
AA 6061	210	18	107

Table 2. Chemical compositions of UNS S33207 and AA 6061, wt. %.

Material	C	Cr	Ni	Mo	Mn	Cu	Co	Si	N	Al	O	Fe
UNS S33207	0.03	26.13	6.31	4.72	1.25	1.02	0.97	0.49	0.38	0.02	0.015	Remaining

Material	Mg	Si	Fe	Cu	Mn	Zn	Ti	Al				
AA 6061	0.92	0.71	0.34	0.30	0.16	0.02	0.01	Remaining				

Materials with a purity of 99.9% were used. The raw materials used were Fe, Co, Ni, Cu, and Mn. These all occupy the fourth period of the periodic table of elements. They share atomic radius, mechanical characteristics, and chemical properties. These elements were anticipated to create a simple phase structure in the HEAs. It has been suggested that HEA systems which include Fe, Co, and Ni often have a high strength-to-ductility ratio. As a result, Fe, Co, Ni, Cu, and Mn were chosen for this experiment. The measured

elements were blended using a ball mill. The powder-mixing tank was cleaned with acetone solution before conducting the experiment. The powder was stirred for more than 10 h. For the proper filling of the HEAs powder, a 30° bevel angle groove was fabricated on the parent metal.

2.2. Laser Welding

In the welding process, a fiber continuous laser welding machine was used (Dong-guan Sanhe, China, model: 3HE-MF1500W, date of manufacture: 2018), and a continuous welding approach was applied. With a purity of 99.9%, argon was used as a shielding gas during welding. The weld parameters were optimized before the experiment with the $Fe_5Co_{20}Ni_{20}Mn_{35}Cu_{20}$ HEAs powders. An ideal set of process parameters was determined and used for welding dissimilar metals of AA 6061 and UNS S33207 alloys, with a 3 mm laser spot diameter, 640 W laser power, and 8 mm/s scanning speed [39,40]. Different parameter combinations were tested in trial runs before finalizing the best combinations [41–43]. Figure 1a shows the laser welding schematic with UNS S33207 hyper-duplex stainless steel (DSS) as the skin and AA 6061 aluminum alloy as the stinger with HEAs filler metal. Figure 1b shows the welded specimen. The laser beam was focused on the butting surface centerline of the lap-joint arrangement. This welding method prevents vaporization, which results in poor weld quality [44]. As a result, the heat generated when the laser beam fell on the HEAs area was effectively carried across the surface of the hyper-duplex steel.
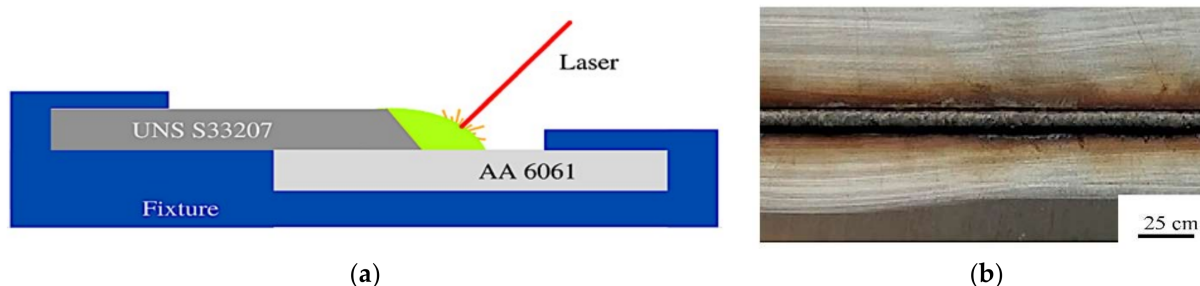

Figure 1. (**a**) Laser welding setup; (**b**) Laser welding plate using HEAs filler.

2.3. Mechanical Testing

Tensile-shear testing was performed to determine the strength of the joints. Straight-sided specimens of 25 mm width and 100 mm length were evaluated according to the ASTM D1002-10 standard. The tests were performed at room temperature with a 1 mm/min crosshead speed. A Zwick Roell tensile testing machine was used to conduct the experiment (Model: ProLine Z005 TN: 2018). Two specimens were prepared using the same parameter combinations, and the average value was taken. Microhardness was also determined at room temperature using a Mitutoyo Micro Vickers hardness testing system (Model: HM-102/103, 2018) as per ASTM E384 standard [45]. Microhardness testing was performed with a load of 25 g for 15 s.

2.4. Materials Characterization

The weld cross-sections were examined to evaluate the weld profile. The cross-sections were placed in epoxy resin and polished using P2000, P1500, P1000, P800, P400, P240 and P100-grit sandpapers with a drum polisher [46]. Keller's and 2% Nital etch solutions were used to etch the aluminum and hyper-duplex stainless-steel surfaces, respectively [47]. To determine the phases present in the base material and weld regions, X-ray diffraction (XRD) was performed (Model No: DW-XRD-27, Make: 2017, Company: Chongqing Drawell Instrument Co., Ltd., Shanghai, China), at 45 kV and 35 mA loaded with a Cu source, which was used as line 0.05° of step size 2θ and 2 s/step.

3. Results and Discussion

Figure 2 shows a cross-section of a laser-welded joint. The composition, fluidity, and surface tension of molten liquid aluminum and high-entropy alloy varied. As a result, it was not necessarily fully mixed, resulting in macro segregation [48,49]. In addition, the shape of the fusion zone on the steel plate indicated conduction welds. The bead geometry also revealed that the depth of diffusion on the steel plate was less than half its thickness, indicating that no molten aluminum was mixed with molten steel during the joining process. The breadth of the aluminum fusion zone, as shown in Figure 2, determined the bonding area between steel and aluminum. The parent material melted acceptably on the hyper-duplex stainless-steel side [50]. As a result, no welding imperfections, such as fractures or pores were prolonged in the joint interface of the weldment. However, after solidification, an HEA zone was formed at the weld interface due to the melting of the HEAs during welding.
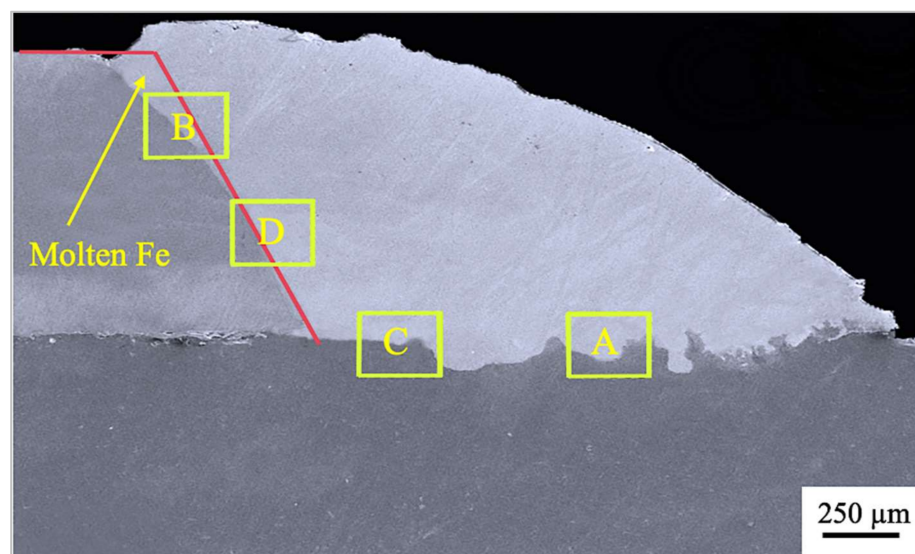

Figure 2. Cross-section of the laser-welded joint. A, B, C and D are the weld zones selected for SEM analysis.

Figure 3 depicts the XRD test results for the $Fe_5Co_{20}Ni_{20}Mn_{35}Cu_{20}$ high-entropy alloy zone. DSS and V solid solutions were the metallographic phases of the high-entropy alloy in the weldment. To limit and control the reactivity of steel and aluminum, a large amount of vanadium was added to the HEAs fillers in the butting surface of the lap joint [51,52]. As a result, the large combining entropy of HEAs was able to improve elemental solubility. In addition, the high blending entropy effect of the HEAs powder produced random solid solutions over IMCs. As a result, the HEAs solidification phase comprised DSS and V solid solutions after welding.

As illustrated in Figure 4, the interaction zone of HEAs/Al is represented in dark grey color; in Figure 5, the HEAs/Fe zone was relatively planar.

The EDS curves at the joint interfaces of the HEAs/Al and HEAs/Fe are shown in Figures 6 and 7. Consistent with the Al-V phase diagram analysis, the EDS curve revealed the substrate at the HEAs/Al joint region, indicating a more significant presence of Al and V. The Al-V IMCs may be dispersed there [53]. The atom intensity of the HEAs/Fe interaction region remained constant. There was no base, which indicated that the atoms in the HEAs/Fe diffused together to generate a layer of diffusion throughout the welding process. In each zone, using EDS analysis, the configurations of the resultant material were measured, and the findings are given in Table 3. At area A in Figure 2, Al and V were 72.34 and 18.27 (wt. %), respectively, and the microstructure was Al_3V. As a result, Al_3V made up most of the multiple layers (nearly all were 0.7 μm) at the interaction zone [54].
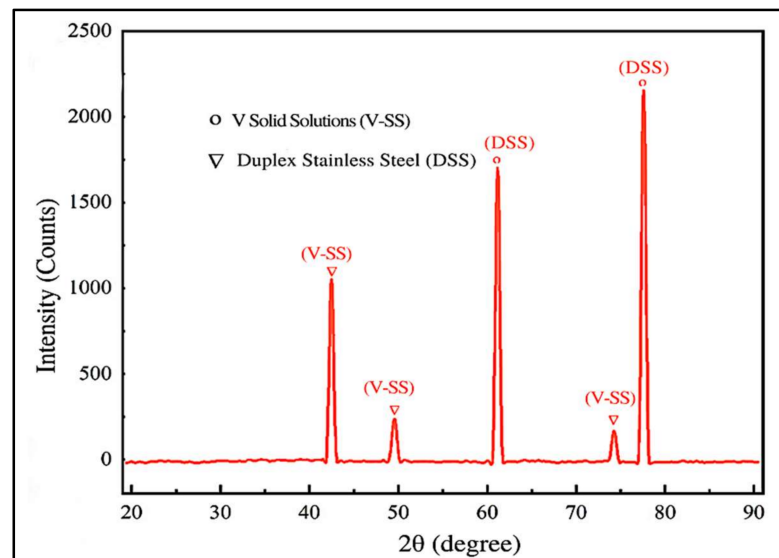
Figure 3. XRD test results for the $Fe_5Co_{20}Ni_{20}Mn_{35}Cu_{20}$ high-entropy alloy zone.
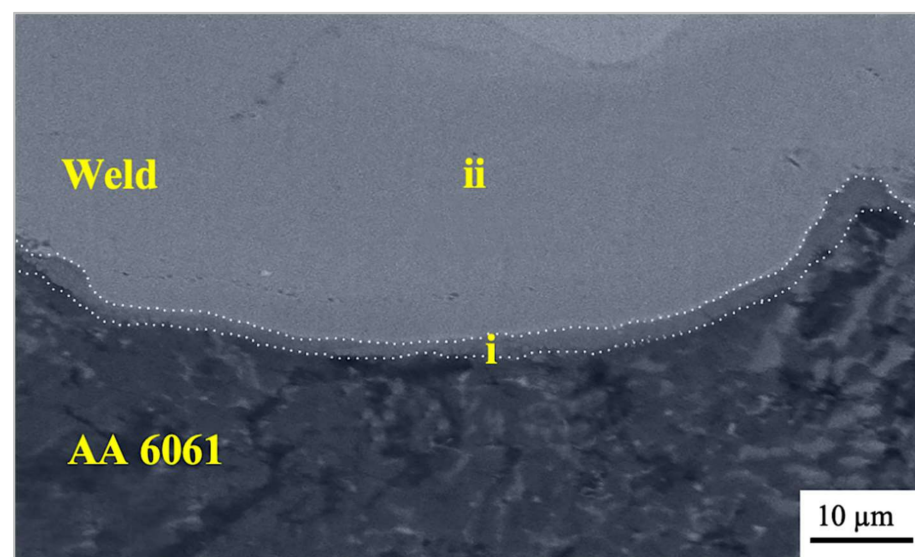

Figure 4. SEM image of weld zone (from area A in Figure 2). i and ii are the areas where EDS performed.

The Al-V IMCs performed effectively at room temperature. No Al element was identified at area B in Figure 2, suggesting that Al element diffusion had been inhibited. Because the HEAs contained many elements, this resulted in substantial lattice deformation in the grain configuration. The kinetic slow diffusion effect, caused by distortion in the structural lattice of HEAs, will obstruct atom mobility [55,56]. Fe atoms visible in area C (Figure 2), but not in area E (Figure 2), indicated a tiny quantity of Fe atoms diffusing to the HEAs with a limited diffusion distance. The HEAs larger mixing entropy can improve element compatibility. A small amount of hyper-duplex stainless steel dispersed into the HEAs without creating any IMCs.
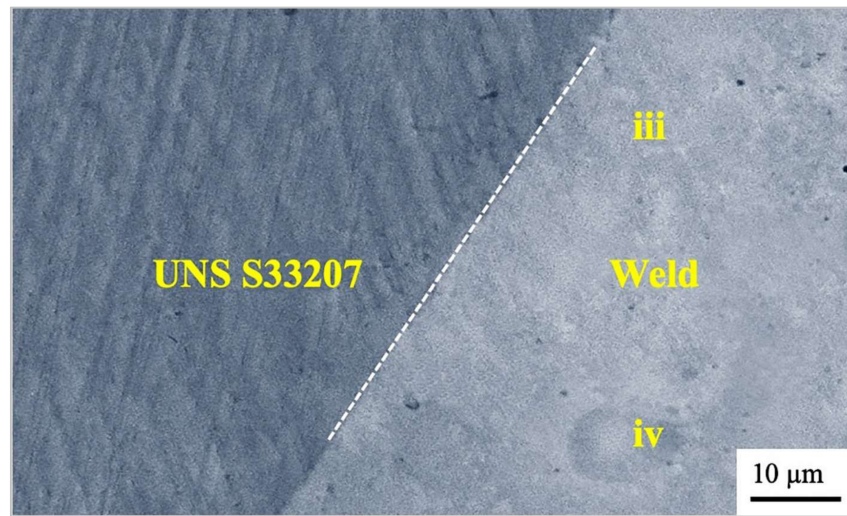
Figure 5. SEM image of the weld zone (from area B in Figure 2). iii and iv are the areas where EDS performed.
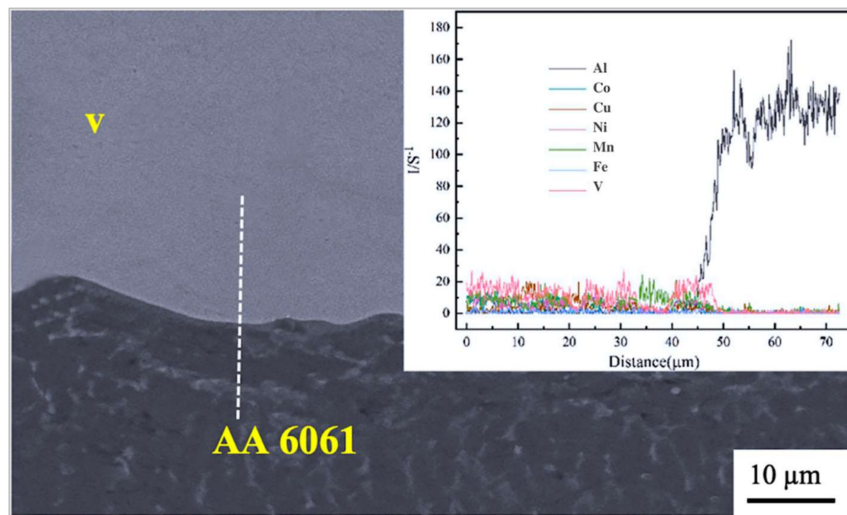

Figure 6. Weld interface SEM image (from area C in Figure 2). v is the areas where EDS performed.
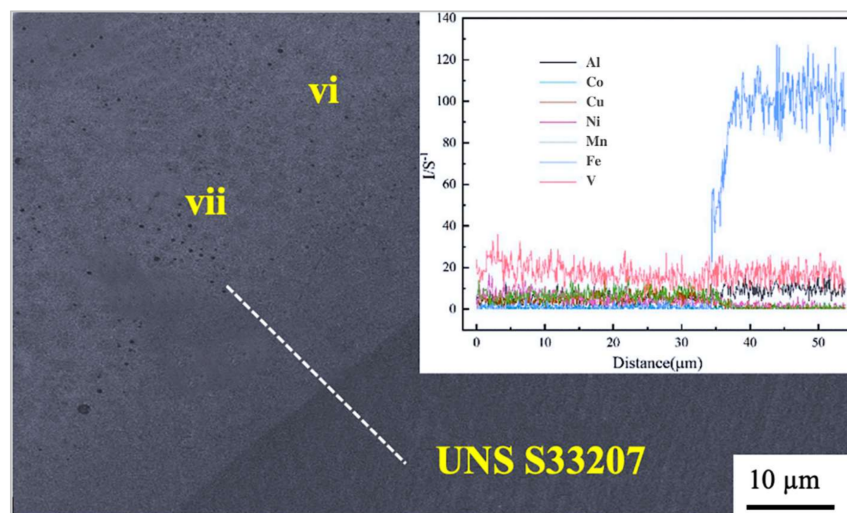

Figure 7. Weld interface SEM image (from area D in Figure 2). vi and vii are the areas where EDS performed.

Table 3. EDS results with respect to different areas in the weld zone.

Area	Composition in Weight%							Related Phases
	Co	**Cu**	**Ni**	**Al**	**Fe**	**V**	**Mn**	
A (i)	0.98	6.21	3.04	68.98	0.00	20.02	1.95	Al_3V
B (ii)	12.98	19.72	14.87	0.00	0.00	29.01	18.71	DCC + V (SS)
C (iii)	11.26	11.98	17.47	0.00	12.21	29.24	19.29	DCC + V (SS)
E (v)	16.02	20.01	15.82	0.00	0.00	28.49	19.82	DCC + V (SS)
G (vii)	-	-	-	-	-	98.63	-	V

Moreover, all materials in the HEAs powder on the Al and Fe sides (indicated as v–vi in Figures 6 and 7) were similar to the HEAs powder used as the filler. The elements Al and Fe were not identified in these areas, showing that using HEAs as a filler prevents the interaction of Al and Fe. The small dark dots in Figures 6 and 7 are vanadium particles (indicated by vii in Figure 7). A small amount of non-melted material particles were identified in the weld interface, which did not influence the joint strength [57]. Figure 8 shows the weld's tensile shear fracture, along with the HEAs/Al interface; this area was the weakest in this joining [58]. The influence of heat and the weak IMC formed between HEAs and Al in this region led to this failure.
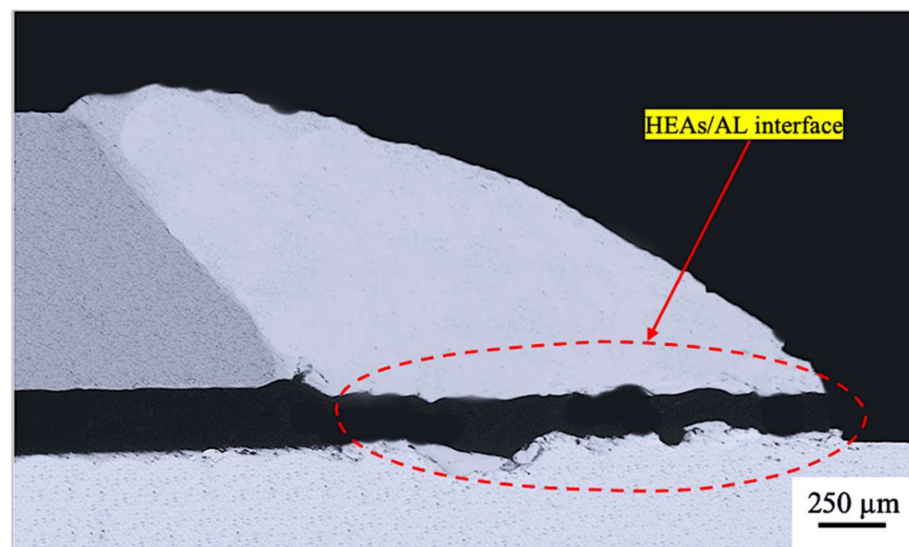
Figure 8. Cross-section of weld fracture.

In Figure 9, all the tensile fractures occurred around the weld interface between the HEAS/Al alloy, and dimples could be seen on the fracture surface, indicating a ductile fracture mechanism for the specimen. When comparing the tensile characteristics of non-filler laser lap welding to the HEAs powder filler induced laser-beam welding, filler-less laser lap welding had a lower tensile shear strength [59,60]. In addition, the on-filler laser lap weld joint's ductility was higher than the HEAs filler-induced laser welding. The latter finding, and the investigation results, suggest that the production of coarse columnar grains in the weld joint reduces ductility.
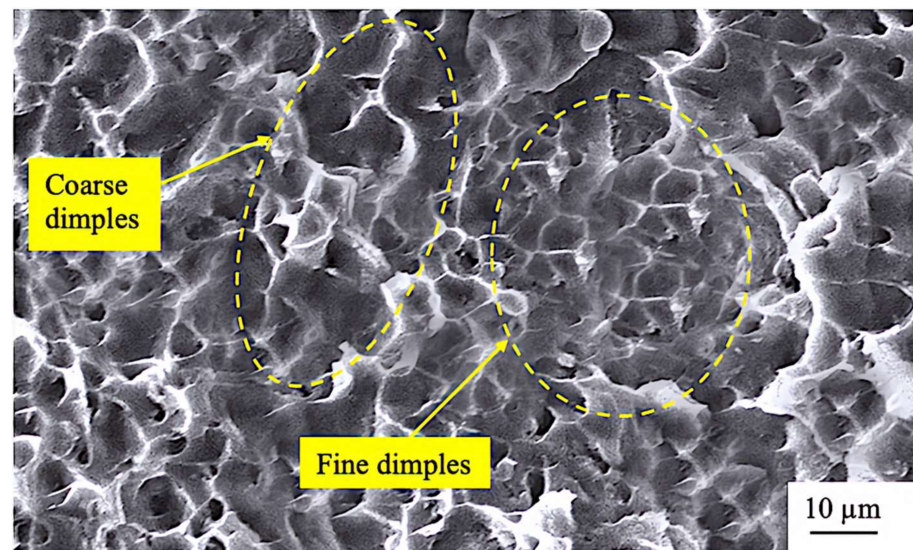
Figure 9. Fracture surface with dimples.

The fracture locations of the tensile-tested parent metal and welds showed that the failure modes were ductile with adequate plastic deformation. Figure 9 shows a significant difference in the size and placement of the dimples on the fracture surface of the joint. The existence of voids and the size variation of the dimples indicated that the ductile fracture occurred with a significant drop in the tensile strength of the laser weld joint [61–63]. Several micro-pores were also identified, which might have been the reason for the lower tensile strength compared to the parent metals. Figure 9 shows a coarse and extended dimple fracture that could break under ductile shear.

The elongated cavities and coarse dimples indicated localized slip, resulting in increased ductility, without lowering the tensile strength of the HEA-induced laser joint. Figure 10 reveals a minor brittle cleavage fracture in the tensile-tested fractography. However, there was a noticeable variation in fracture patterns.
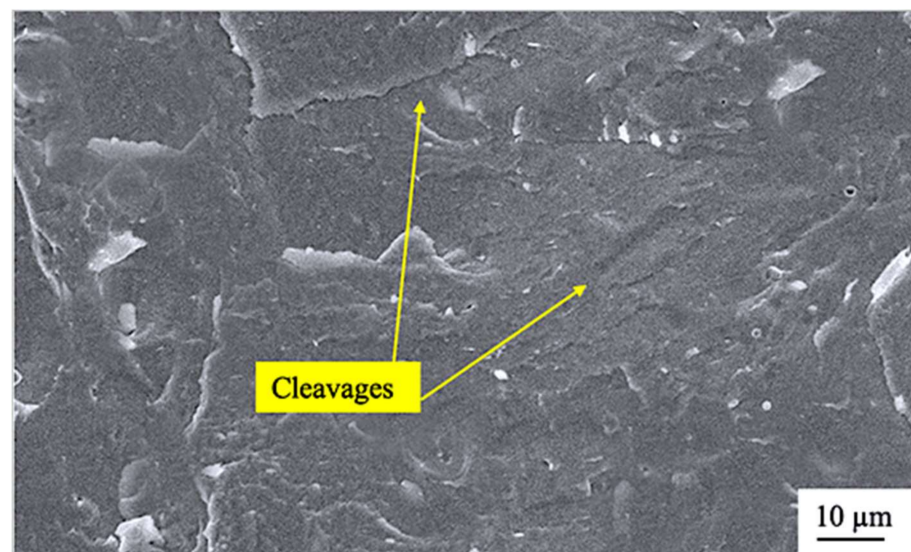

Figure 10. Cleavage surface.

The predominant properties of the HEAs filler and fine secondary dimples enhanced the tensile strength of the HEAs-filler-induced laser joint. The fractography (Figures 8–10) illustrates the specimen's ductile and brittle fracture properties [64]. The presence of the

Al$_3$V phase was verified using XRD data from the fracture cross-section, as shown in Figure 11.
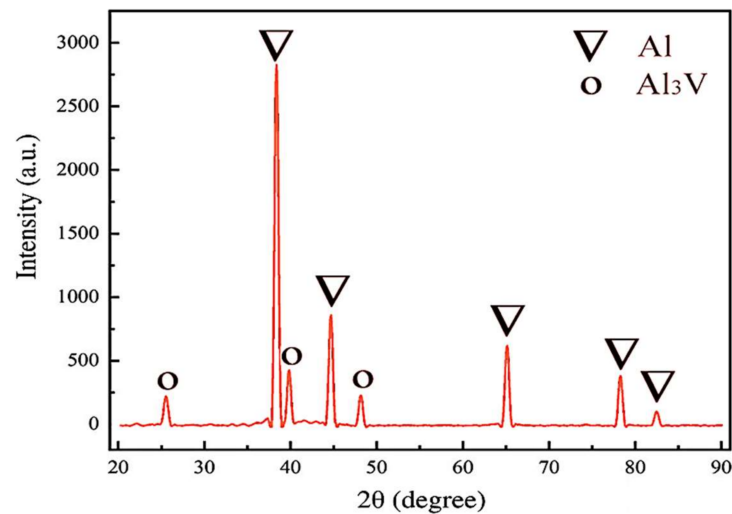

Figure 11. XRD data from fracture cross-section.

Figure 12 shows the tensile stress-strain curve at room temperature for the HEAs-powder-filler-induced laser welding. The tensile fracture was prolonged at the weldment's HEAs/Al metal interface. The weld had a tensile strength of 237 MPa. This highlighted that the weld joint had lower tensile strength than one of the base metals UNS S33207 hyper-duplex stainless steel and higher tensile strength than the aluminum alloy Al 6061. The noise observed in the stress-strain graph was caused by the HEAs' constant emergence of different phases. These different regions were: a linear elastic area, a tiny plastic region, and a further linear elastic region followed by plastic deformation [65]. As previously observed, coarse columnar grains in the joint region resulted in poorer ductility than fine equiaxed refined microstructure [66,67].
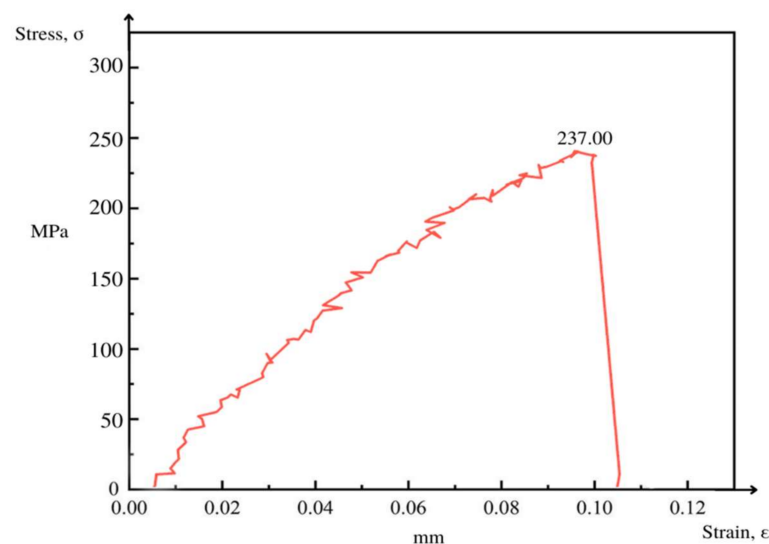

Figure 12. Tensile stress-strain curve.

The Vicker's microhardness profile for the joint cross-section is given in Figure 13. The results showed that the average microhardness achieved in the weld zone where HEAs filler was deposited was 674 HV. However, the highest microhardness achieved in the weld zone where the HEAs/Fe interaction occurred was 693 HV, and in the HEAs

region was 703 HV. The HEAs/Al weld interface evidenced a microhardness of 207 HV. Hence, the shear-transformed DSS phase with Al_3V and V solid solutions transformed the post-weld microstructure of the weld zone [68,69]. Higher microhardness values in the weld zone might have been due to this phase transformation. The welded joints' hardness profiles (shown in Figure 13) are consistent with the joint's resultant tensile shear strength characteristics.
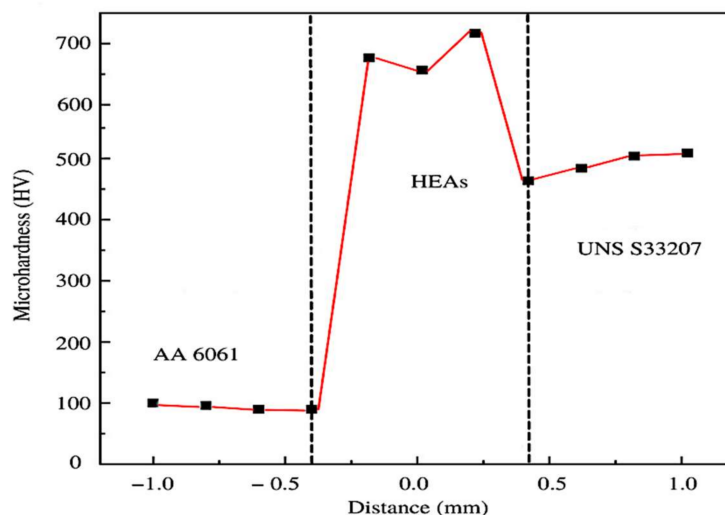

Figure 13. Microhardness profile from the welded joint cross-section.

4. Conclusions

It is well established that intermetallic compound layer thickness, phase transformations and area of bonding have an overriding influence on the mechanical and metallurgical properties of welding using stainless steel and aluminum alloys. In this investigation, a high entropy alloys powder was chosen as a filler for laser welding. The conclusions derived from this research are as given below:

1. In this laser welding experiment for joining UNS S33207 to aluminum alloy 6061, $Fe_5Co_{20}Ni_{20}Mn_{35}Cu_{20}$ HEAs powder was chosen as the lap welding filler.
2. The Fe and Al alloy's mutual mixing and reaction were prevented by monitoring the melting quantity of the parent metal in the hyper-duplex stainless-steel side. Al/Fe intermetallic compounds were not identified in the joints weld zone.
3. The metallographic phases identified for the HEAs in the weld region were DSS and V solid solutions.
4. The large entropy property of HEAs favored the production of arbitrary solid solutions over IMCs. As a result, the HEAs' after-melting phase was comprised of DSS and V solid solutions.
5. Fractography revealed mostly fine dimples, with a few coarse dimples also visible.
6. The weld had a tensile strength of 237 MPa, and the tensile fracture was prolonged at the joint's HEAs/Al metal interface.
7. The highest microhardness achieved in the weld zone was at the HEAs/Fe interaction area, which was 703 HV, with the HEAs/ Al weld interface having a microhardness of 207 HV.

References

1. Pańcikiewicz, K.; Świerczyńska, A.; Hućko, P.; Tumidajewicz, M. Laser Dissimilar Welding of AISI 430F and AISI 304 Stainless Steels. *Materials* **2020**, *13*, 4540. [CrossRef] [PubMed]
2. Landowski, M.; Świerczyńska, A.; Rogalski, G.; Fydrych, D. Autogenous Fiber Laser Welding of 316L Austenitic and 2304 Lean Duplex Stainless Steels. *Materials* **2020**, *13*, 2930. [CrossRef] [PubMed]
3. Lin, C.; Shiue, R.-K.; Wu, S.-K.; Huang, H.-L. Infrared Brazing of CoCrFeMnNi Equiatomic High Entropy Alloy Using Nickel-Based Braze Alloys. *Entropy* **2019**, *21*, 283. [CrossRef] [PubMed]
4. Jiang, P.; Chen, R. Research on Interfactial Layer of Laser-Welded Aluminum to Titanium. *Mater. Charact.* **2019**, *154*, 264–268. [CrossRef]
5. Borrisutthekul, R.; Yachi, T.; Miyashita, Y.; Mutoh, Y. Suppression of Intermetallic Reaction Layer Formation by Controlling Heat Flow in Dissimilar Joining of Steel and Aluminum Alloy. *Mater. Sci. Eng. A* **2007**, *467*, 108–113. [CrossRef]
6. Bouche, K.; Barbier, F.; Coulet, A. Intermetallic Compound Layer Growth Between Solid Iron and Molten Aluminium. *Mater. Sci. Eng. A* **1998**, *249*, 167–175. [CrossRef]
7. Colegrove, P.; Williams, S.W.; Ikeagu, C.; Thistlethwaite, A. The Impact of Different Types of Welding Processes on the Residual Stress and Distortion in 4 mm Thick Butt Welds of Ship Plate. In *Trends in Welding Research: Proceedings of the 8th International Conference. ASM International Georgia, USA*; David, S.A., DebRoy, T., DuPont, J.N., Koseki, T., Smartt, H.B., Eds.; ASM International: Materials Park, OH, USA, 2009; pp. 758–765.
8. He, Z.; Sun, L.; Li, C.; Si, X.; Zhang, C.; Qi, J.; Feng, J.; Cao, J. Wetting and Brazing of Cf/C Composite with Si–Zr Eutectic Alloy: The formation of nano-and coarse-SiC reaction layers. *Carbon* **2020**, *167*, 92–103. [CrossRef]
9. Ding, J.; Colegrove, P.; Mehnen, J.; Ganguly, S.; Almeida, P.M.S.; Wang, F.; Williams, S. Thermo-mechanical Analysis of Wire and Arc Additive Layer Manufacturing Process on Large Multi-layer Parts. *Comput. Mater. Sci.* **2011**, *50*, 3315–3322. [CrossRef]
10. Górka, J. Assessment of the Effect of Laser Welding on the Properties and Structure of TMCP Steel Butt Joints. *Materials* **2020**, *13*, 1312. [CrossRef]
11. Lisiecki, A.; Ślizak, D. Hybrid Laser Deposition of Composite WC-Ni Layers with Forced Local Cryogenic Cooling. *Materials* **2021**, *14*, 4312. [CrossRef]
12. Kotarska, A.; Poloczek, T.; Janicki, D. Characterization of the Structure, Mechanical Properties and Erosive Resistance of the Laser Cladded Inconel 625-Based Coatings Reinforced by TiC Particles. *Materials* **2021**, *14*, 2225. [CrossRef] [PubMed]
13. Kik, T. Heat Source Models in Numerical Simulations of Laser Welding. *Materials* **2020**, *13*, 2653. [CrossRef] [PubMed]
14. Lubas, J.; Szczypiński-Sala, W.; Woś, P.; Zielińska, E.; Miernik, K. Experimental Analysis of Tribological Processes in Friction Pairs with Laser Borided Elements Lubricated with Engine Oils. *Materials* **2020**, *13*, 5810. [CrossRef] [PubMed]
15. Luo, Y.; Jiang, W.; Zhang, W.; Zhang, Y.; Woo, W.; Tu, S. Notch effect on creep damage for Hastelloy C276-BNi2 brazing joint. *Mater. Des.* **2015**, *84*, 212–222. [CrossRef]
16. Fan, J.; Thomy, C.; Vollertsen, F. Effect of Thermal Cycle on the Formation of Intermetallic Compounds in Laser Welding of Aluminum-Steel Overlap Joints. *Phys. Proced.* **2011**, *12*, 134–141. [CrossRef]
17. Urbańczyk, M.; Adamiec, J. Hybrid Welding (Laser–Electric Arc MAG) of High Yield Point Steel S960QL. *Materials* **2021**, *14*, 5447. [CrossRef]
18. Czupryński, A. Comparison of Properties of Hardfaced Layers Made by a Metal-Core-Covered Tubular Electrode with a Special Chemical Composition. *Materials* **2020**, *13*, 5445. [CrossRef]
19. Walczak, M.; Szala, M. Effect of Shot Peening on the Surface Properties, Corrosion and Wear Performance of 17-4PH Steel Produced by DMLS Additive Manufacturing. Archiv. *Civ. Mech. Eng.* **2021**, *21*, 157. [CrossRef]
20. Rahman Rashid, R.A.; Nazari, K.A.; Barr, C.; Palanisamy, S.; Orchowski, N.; Matthews, N.; Dargusch, M.S. Effect of Laser Reheat Post-treatment on the Microstructural Characteristics of Laser-Cladded Ultra-High Strength Steel. *Surf. Coat. Technol.* **2019**, *372*, 93–102. [CrossRef]
21. Majkowska-Marzec, B.; Tęczar, P.; Bartmański, M.; Bartosewicz, B.; Jankiewicz, B.J. Mechanical and Corrosion Properties of Laser Surface-Treated Ti13Nb13Zr Alloy with MWCNTs Coatings. *Materials* **2020**, *13*, 3991. [CrossRef]

22. Jażdżewska, M.; Kwidzińska, D.B.; Seyda, W.; Fydrych, D.; Zieliński, A. Mechanical Properties and Residual Stress Measurements of Grade IV Titanium and Ti-6Al-4V and Ti-13Nb-13Zr Titanium Alloys after Laser Treatment. *Materials* **2021**, *14*, 6316. [CrossRef] [PubMed]

23. Fu, Y.; Guo, N.; Zhou, C.; Wang, G.; Feng, J. Investigation on In-situ Laser Cladding Coating of the 304 Stainless Steel in Water Environment. *J. Mater. Process. Technol.* **2021**, *289*, 116849. [CrossRef]

24. Hwang, T.W.; Han, S.W.; Lee, T.; Kim, J.H.; Van Tyne, C.J.; Moon, Y.H. Underwater Surface Remelting of Selective Laser Melted Titanium Parts. *J. Mater. Res. Technol.* **2020**, *9*, 10447–10458. [CrossRef]

25. Kim, D.; Badarinarayan, H.; Kim, J.H.; Kim, C.; Okamoto, K.; Wagoner, R.H.; Chung, K. Numerical Simulation of Friction Stir Butt Welding Process for AA5083-H18 Sheets. *Eur. J. Mech. A Solids* **2010**, *29*, 204–215. [CrossRef]

26. Olson, D.L. *ASM Handbook Volume 6: Welding, Brazing and Soldering*; ASM International: Cleveland, OH, USA, 1993; p. 2603.

27. Danielewski, H.; Skrzypczyk, A. Steel Sheets Laser Lap Joint Welding—Process Analysis. *Materials* **2020**, *13*, 2258. [CrossRef]

28. Ma, J.; Harooni, M.; Carlson, B.; Kovacevic, R. Dissimilar Joining of Galvanized High-strength Steel to Aluminum Alloy in a Zero-gap Lap Joint Configuration by Two-pass Laser Welding. *Mater. Des.* **2014**, *58*, 390–401. [CrossRef]

29. Liu, H.; Xin, C.; Liu, L.; Zhuang, C. Effects of Different Contents of Each Component on the Structural Stability and Mechanical Properties of Co-Cr-Fe-Ni High-Entropy Alloys. *Appl. Sci.* **2021**, *11*, 2832. [CrossRef]

30. Zhu, J.; Fu, H.; Zhang, H.; Wang, A.; Li, H.; Hu, Z. Microstructure and Compressive Properties of Multiprincipal Component AlCoCrFeNiCx Alloys. *J. Alloys Compd.* **2011**, *509*, 3476–3480. [CrossRef]

31. Yeh, J.W. Alloy Design Strategies and Future Trends in High-Entropy Alloys. *JOM* **2013**, *65*, 1759–1771. [CrossRef]

32. Mathieu, A.; Shabadi, R.; Deschamps, A.; Suery, M.; Matteı, S.; Grevey, D.; Cicala, E. Dissimilar Material Joining Using Laser (Aluminum to Steel using Zinc-based Filler Wire). *Opt. Laser Technol.* **2007**, *39*, 652–661. [CrossRef]

33. Cantor, B. Multicomponent and High Entropy Alloys. *Entropy* **2014**, *16*, 4749. [CrossRef]

34. Meco, S.; Ganguly, S.; Williams, S.; McPherson, N. Effect of Laser Processing Parameters on the Formation of Intermetallic Compounds in Fe-Al Dissimilar Welding. *J. Mater. Eng. Perform.* **2014**, *23*, 3361–3370. [CrossRef]

35. Ozaki, H.; Kutsuna, M. Laser-roll Welding of a Dissimilar Metal Joint of Low Carbon Steel to Aluminium Alloy Using 2 kW Fibre Laser. *Weld. Int.* **2009**, *23*, 345–352. [CrossRef]

36. Quintino, L.; Assunção, E. Conduction laser welding. In *Handbook of Laser Welding Technologies*; Katayama, S., Ed.; Woodhead Publishing: Sawston, UK, 2013; pp. 139–162. [CrossRef]

37. Schubert, E.; Zerner, I.; Sepold, G. Laser beam joining of material combinations for automotive applications. *Lasers Mater. Process.* **1997**, *3097*, 212–221. [CrossRef]

38. Shahverdi, H.R.; Ghomashchi, M.R.; Shabestari, S.; Hejazi, J. Microstructural Analysis of Interfacial Reaction between Molten Aluminium and Solid Iron. *J. Mater. Process. Technol.* **2002**, *124*, 345–352. [CrossRef]

39. Vemanaboina, H.; Gundabattini, E.; Akella, S.; Rao, A.C.U.M.; Buddu, R.K.; Ferro, P.; Berto, F. Mechanical and Metallurgical Properties of CO_2 Laser Beam INCONEL 625 Welded Joints. *Appl. Sci.* **2021**, *11*, 7002. [CrossRef]

40. Chludzinski, M.; dos Santos, R.E.; Churiaque, C.; Ortega-Iguña, M.; Sánchez-Amaya, J.M. Pulsed Laser Welding Applied to Metallic Materials—A Material Approach. *Metals* **2021**, *11*, 640. [CrossRef]

41. Lopes, J.G.; Oliveira, J.P. A Short Review on Welding and Joining of High Entropy Alloys. *Metals* **2020**, *10*, 212. [CrossRef]

42. Pereira, A.B.; Cabrinha, A.; Rocha, F.; Marques, P.; Fernandes, F.A.O.; Alves de Sousa, R.J. Dissimilar Metals Laser Welding between DP1000 Steel and Aluminum Alloy 1050. *Metals* **2019**, *9*, 102. [CrossRef]

43. Springer, H.; Kostka, A.; Payton, E.J.; Raabe, D.; Kaysser-Pyzalla, A.; Eggeler, G. On the formation and growth of intermetallic phases during interdiffusion between lowcarbon steel and aluminum alloys. *Acta Mater.* **2011**, *59*, 1586–1600. [CrossRef]

44. Mohan, D.G.; Tomków, J.; Gopi, S. Induction Assisted Hybrid Friction Stir Welding of Dissimilar MaterialsAA5052 Aluminium Alloy and X12Cr13 Stainless Steel. *Adv. Mater. Sci.* **2021**, *21*, 17–30. [CrossRef]

45. Suder, W.J.; Williams, S.W. Investigation of the Effects of Basic Laser Material Interaction Parameters in Laser Welding. *J. Laser Appl.* **2012**, *24*, 032009. [CrossRef]

46. Wang, X.; Wood, J.V.; Sui, Y.; Lu, H. Formation of Intermetallic Compound in Ironaluminum Alloys. *J. Shanghai Univ. (Engl. Ed.)* **1998**, *2*, 305–310. [CrossRef]

47. AnandhaKumar, C.J.; Gopi, S.; Mohan, D.G.; ShashiKumar, S. Predicting the Ultimate Tensile Strength and Wear Rate of Aluminium Hybrid Surface Composites Fabricated via Friction Stir Processing Using Computational Methods. *J. Adhes. Sci. Technol.* **2021**, 1–20. [CrossRef]

48. Bi, J.; Lei, Z.; Chen, Y.; Chen, X.; Tian, Z.; Liang, J.; Qin, X.; Zhang, X. Densification, Microstructure and Mechanical Properties of an Al-14.1Mg-0.47Si-0.31Sc-0.17Zr Alloy Printed by Selective Laser Melting. *Mater. Sci. Eng. A* **2020**, *774*, 138931. [CrossRef]

49. Zhu, Z.; Wang, W.; Li, Y.; Chen, H. Effect of Laser-arc Offset and Laser-deviation Angle on the Control of a Ti-Al Interlayer. *J. Mater. Process. Technol.* **2019**, *271*, 336–345. [CrossRef]

50. Way, M.; Luo, D.; Tuley, R.; Goodall, R. A new High Entropy Alloy Brazing Filler Metal Design for Joining Skutterudite Thermoelectrics to Copper. *J. Alloys Compd.* **2020**, *858*, 157750. [CrossRef]

51. Mohan, D.G.; Gopi, S.; Tomków, J.; Memon, S. Assessment of Corrosive Behaviour and Microstructure Characterization of Hybrid Friction Stir Welded Martensitic Stainless Steel. *Adv. Mater. Sci.* **2021**, *21*, 67–78. [CrossRef]

52. Cao, J.; Zhang, L.; Wang, H.; Wu, L.; Feng, J. Effect of Silver Content on Microstructure and Properties of Brass/steel Induction Brazing Joint Using Ag-Cu-Zn-Sn Filler Metal. *J. Mater. Sci. Technol.* **2011**, *27*, 377–381. [CrossRef]

53. Quazi, M.M.; Ishak, M.; Fazal, M.A.; Arslan, A.; Rubaiee, S.; Qaban, A.; Aiman, M.H.; Sultan, T.; Ali, M.M.; Manladan, S.M. Current research and development status of dissimilar materials laser welding of titanium and its alloys. *Opt. Laser Technol.* **2020**, *126*, 106090. [CrossRef]

54. Tomashchuk, I.; Sallamand, P.; Measson, A.; Cicala, E.; Duband, M.; Peyre, P.J. Aluminum to Titanium Laser Welding-brazing in V-shaped Groove. Mater. *Process. Technol.* **2017**, *245*, 24–36. [CrossRef]

55. Song, Z.; Nakata, K.; Wu, A.; Liao, J. Interfacial Microstructure and Mechanical Property of Ti6Al4V/A6061 Dissimilar Joint by Direct Laser Brazing without Filler Metal and Groove. *Mater. Sci. Eng. A* **2013**, *560*, 111–120. [CrossRef]

56. Glowka, K.; Zubko, M.; Świec, P.; Prusik, K.; Szklarska, M.; Chrobak, D.; Lábár, J.L.; Stróż, D. Influence of Molybdenum on the Microstructure, Mechanical Properties and Corrosion Resistance of Ti20Ta20Nb20(ZrHf)20−xMox (Where: x = 0, 5, 10, 15, 20) High Entropy Alloys. *Materials* **2022**, *15*, 393. [CrossRef] [PubMed]

57. Sharma, A. High-Entropy Alloys for Micro- and Nanojoining Applications. In *Engineering Steels and High Entropy-Alloys*; IntechOpen: London, UK, 2020.

58. Mohan, D.G.; Gopi, S. Influence of In-situ Induction Heated Friction Stir Welding on Tensile, Microhardness, Corrosion Resistance and Microstructural Properties of Martensitic Steel. *Eng. Res. Express* **2021**, *3*, 25023. [CrossRef]

59. Tomashchuk, I.; Sallamand, P.; Cicala, E.; Peyre, P.; Grevey, D. Direct Keyhole Laser Welding of Aluminum Alloy AA5754 to Titanium Alloy Ti6Al4V. *J. Mater. Process. Technol.* **2015**, *217*, 96–104. [CrossRef]

60. Chen, S.-H.; Li, L.-Q.; Chen, Y.-B.; Liu, D.-J. Si Diffusion Behavior During Laser Welding-brazing of Al alloy and Ti Alloy with Al-12Si Filler Wire. *Trans. Nonferrous Met. Soc. China* **2010**, *20*, 64–70. [CrossRef]

61. Menci, G.; Demir, A.G.; Waugh, D.G.; Lawrence, J.; Previtali, B. Laser Surface Texturing of β-Ti alloy for Orthopaedics: Effect of Different Wavelengths and Pulse Durations. *Appl. Surf. Sci.* **2019**, *489*, 175–186. [CrossRef]

62. Liaw, P.K.; Li, W. High Entropy Materials: Challenges and Prospects. *Metals* **2021**, *11*, 1643. [CrossRef]

63. Hardwick, L.; Rodgers, P.; Pickering, E. Development of Novel Nickel-based Brazing Alloys, Utilisingutilising Alternative Melting Point Depressants and High Entropy Alloy Concepts. In Proceedings of the 12th International Conference on Brazing, High Temperature Brazing and Diffusion Bonding, Aachen, Germany, 21–23 May 2019.

64. Zhang, Y.; Sun, D.Q.; Gu, X.Y.; Duan, Z.Z.; Li, H.M. Nd:YAG Pulsed Laser Welding of TC$_4$ Ti alloy to 301L Stainless Steel using Ta/V/Fe Composite Interlayer. *Mater. Lett.* **2018**, *212*, 54–57. [CrossRef]

65. Meraj, M.; Pal, S. Deformation of Ni$_{20}$W$_{20}$Cu$_{20}$Fe$_{20}$Mo$_{20}$ High Entropy Alloy for Tensile followed by Compressive and Compressive followed by Tensile Loading: A Molecular Dynamics Simulation Based Study. *IOP Conf. Ser. Mater. Sci. Eng.* **2019**, *115*, 012019. [CrossRef]

66. Luo, D.; Xiao, Y.; Hardwick, L.; Snell, R.; Way, M.; Sanuy Morell, X.; Livera, F.; Ludford, N.; Panwisawas, C.; Dong, H.; et al. High Entropy Alloys as Filler Metals for Joining. *Entropy* **2021**, *23*, 78. [CrossRef] [PubMed]

67. Liu, D.; Wang, J.; Xu, M.; Jiao, H.; Tang, Y.; Li, D.; Zhao, L.; Han, S. Evaluation of Dissimilar Metal Joining of Aluminum Alloy to Stainless Steel using the Filler Metals with a High-entropy Design. *J. Manuf. Process.* **2020**, *58*, 500–509. [CrossRef]

68. Fu, A.; Cao, Y.; Liu, Y.; Xu, S. Microstructure and Mechanical Properties of Novel Lightweight TaNbVTi-Based Refractory High Entropy Alloys. *Materials* **2022**, *15*, 355. [CrossRef] [PubMed]

69. Meng, F.S.; Yao, Z.; Všianská, M.; Friák, M.; Šob, M. Theoretical Investigations on Structural, Elastic, Thermodynamic and Electronic Properties of Al$_3$Ti and Al$_3$V Compounds in L$_{12}$ Structure under High Pressure. *Mater. Res. Express* **2019**, *6*, 056536. [CrossRef]